

Composition-Tuned ZnO–CdSSe Core–Shell Nanowire Arrays

Yoon Myung, Dong Myung Jang, Tae Kwang Sung, Yong Jei Sohn, Gyeong Bok Jung, Yong Jae Cho, Han Sung Kim, and Jeunghee Park*

Department of Chemistry, Korea University, Jochiwon 339-700, Korea

Solar-energy conversion into electricity is fast becoming a vital source of renewable energy and is being developed as an alternative to traditional fossil fuel-based sources of power. One promising device for inexpensive, large-scale solar energy conversion is the TiO_2 -based photoelectrochemical cell (PEC), which was first discovered by Fujishima and Honda using UV irradiation.¹ To improve the performance of PECs in the visible light region, the development of smaller band gap materials or new architectures is required, which represents a serious technological challenge. In particular, novel photoelectrodes in which arrays of TiO_2 or ZnO one-dimensional (1-D) nanostructures (e.g., nanorods, nanowires, or nanotubes) are grown on a conducting substrate are emerging as an alternative to nanocrystalline TiO_2 films.^{2–9} They can help to improve the electron transport by avoiding the particle-to-particle hopping that occurs in the TiO_2 network. Furthermore, their 1-D nanostructure morphology can increase the likelihood that all photogenerated electrons have a direct connection to the collection electrode. In previous studies, they were photosensitized with various semiconductor nanocrystals (or quantum dots), for example, CdS ,^{10–20} CdSe ,^{20–26} CdTe ,^{27,28} ZnSe ,²⁹ Cu_2O ,³⁰ and CuInS_2 ,³¹ showing efficient photocurrent generation under visible light irradiation.

A number of works have demonstrated the advantage of the core–shell nanowire architecture, in which carrier separation takes place in the radial *versus* the longer axial direction, with a carrier collection distance smaller or comparable to the minority carrier diffusion length.^{32–38} Building from these ideas, herein we examine an

ABSTRACT Vertically aligned ZnO – CdSSe core–shell nanowire arrays were synthesized with a controlled composition and shell thickness (10–50 nm) by the chemical vapor deposition on the pregrown ZnO nanowire arrays. They consisted of a composition-tuned single-crystalline wurtzite structure $\text{CdS}_{1-x}\text{Se}_x$ ($x = 0, 0.5$, and 1) shell whose [0001] direction was aligned along the [0001] wire axis of the wurtzite ZnO core. The analysis of structural and optical properties shows the formation of Zn containing alloy in the interface region between the ZnO core and shell, which can facilitate the growth of single-crystalline shell layers by reducing both the lattice mismatch and the number of defect sites. In contrast, the TiO_2 (rutile) nanowire array can form the polycrystalline shell under the same condition. The photoelectrochemical cell using the ZnO – CdS photoelectrode exhibits a higher photocurrent and hydrogen generation rate than that using the TiO_2 – CdS one. We suggest that the formation of the CdZnSSe intermediate layers contributes to the higher photoelectrochemical cell performance of the ZnO – CdSSe nanowires.

KEYWORDS: ZnO · CdSSe · chemical vapor deposition · core–shell nanowires · photoelectrochemical cell

array of ZnO and TiO_2 nanowire (NW) cores photosensitized with CdSSe nanocrystal shells, as a promising photoelectrode architecture. Because of the presence of nanometer-size heterointerface between the semiconductor shell and the NW core, it provides significant advantages both for light absorption and for charge separation, which are two critical steps in solar-to-electric energy conversion. In the present study, we synthesized ZnO – CdSSe core–shell nanowire (NC) arrays with a controlled composition and thickness of the shell, using a relatively simple and low-cost approach, *viz.* the chemical vapor deposition (CVD) method. The present result will demonstrate a great advantage of CVD method, which enables an epitaxial growth of the composition-tuned single-crystalline shell on the ZnO NW core. The composition tuning of CdSSe shell and their light emission using the CVD method were demonstrated for the Si NWs.³⁹ There is a report for $\text{CdS}_{0.7}\text{Se}_{0.3}$ quantum dots– TiO_2 nanobelts composites and photocurrents.²⁰

*Address correspondence to parkjh@korea.ac.kr.

Received for review February 11, 2010 and accepted June 02, 2010.

Published online June 7, 2010.
10.1021/nn100684q

© 2010 American Chemical Society

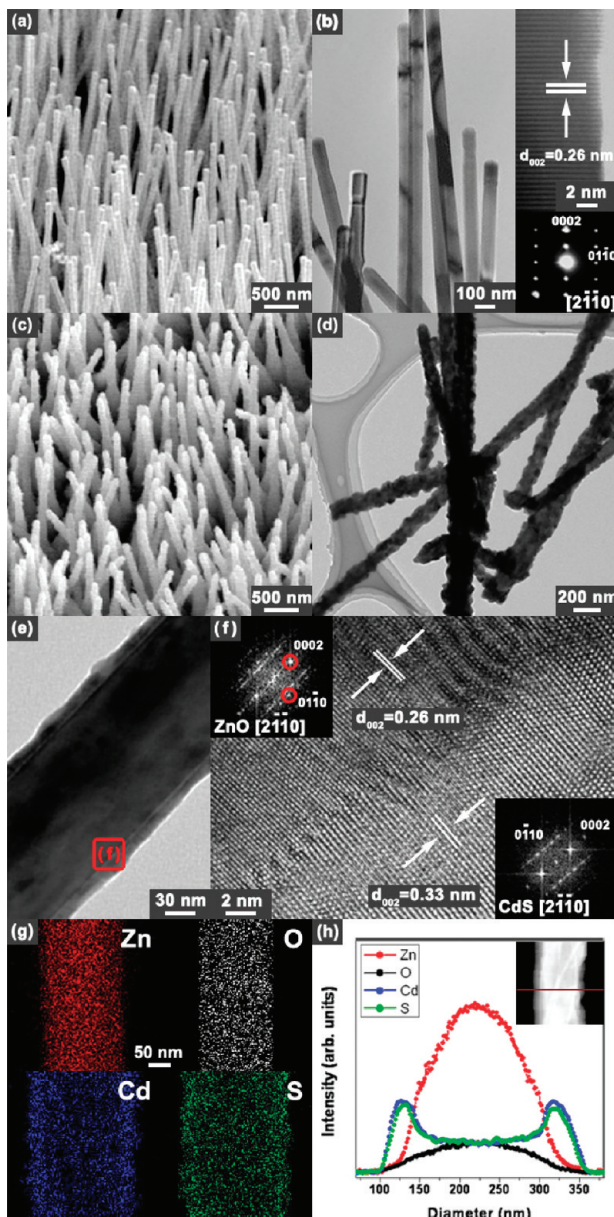


Figure 1. (a) SEM micrograph of the high-density vertically aligned ZnO NW array on the Ti substrate. (b) TEM image showing the uniform diameter (80 nm) of the ZnO NWs. Lattice-resolved image and its corresponding SAED pattern, showing the single-crystalline wurtzite ZnO NW grown along the [0001] direction (insets). (c) SEM micrograph of the ZnO–CdS (ZC2) array grown on the Ti substrate. TEM images showing the ZnO–CdS having (d) 50 nm– (ZC2) and (e) 10 nm-thick CdS shells (ZC1). (f) The lattice-resolved image of the interface region (ZC1) shows that the [0001] direction of the single-crystalline wurtzite CdS is aligned along the [0001] wire axis of ZnO. Its corresponding FFT ED pattern confirms the alignment of the [0001] direction of the CdS and ZnO (insets). The EDX elemental (g) mapping and (h) line-scan reveal the presence of Zn and O elements in the core part, and Cd and S elements in the shell part. The STEM image is shown in the inset.

However, to our best knowledge, no attempts have been made to synthesize composition-tuned CdS-shelled ZnO NC arrays using the CVD method.

We characterized their structural and optical properties by applying a comprehensive set of techniques, showing the formation of Zn containing al-

loy in the interface region between the ZnO core and single-crystalline CdSSe shell. PECs were designed using these NC array electrodes, to achieve photocurrent and H₂ generation under visible light irradiation. We showed the higher photoconversion efficiency of the ZnO–CdS NCs than that of the TiO₂–CdS ones, having a polycrystalline shell, which were grown using the same CVD method. The successful achievement of such PECs would be a key step toward the demonstration of a new viable nanometer-scale solar cell technology.

RESULTS AND DISCUSSION

Synthesis of ZnO–CdS core–shell NCs. Figure 1a shows a SEM image of the vertically aligned ZnO NW array (length = ~10 μm) grown on the Ti substrates. The TEM image reveals that the average diameter of the ZnO NWs is 80 nm (Figure 1b). The two insets show the HRTEM image and its corresponding selected-area electron diffraction (SAED) pattern for a selected NW, confirming the formation of single-crystalline wurtzite ZnO crystals grown with the [0001] direction. The (002) fringes are separated by a distance of about 2.6 Å, which is close to that of the bulk (JCPDS Card No. 36-1451; $a = 3.24982$ Å, $c = 5.20661$ Å).

We synthesized ZnO–CdS NC samples having 10 (± 5) nm- and 50 (± 10) nm-thick CdS outerlayers, and referred to them as “ZC1” and “ZC2”, respectively. Figure 1c shows a SEM image of the ZnO–CdS NC (ZC2) array, in which the CdS layers were deposited using the CVD method.⁴⁰ The use of a higher deposition temperature or longer time increases the thickness of the CdS shell. The deposition of thicker CdS layers makes the surface more rough. The TEM image of the ZC2 reveals its nanocable morphology, in which the rough-surface outerlayers are coated along the entire length of the ZnO NWs (Figure 1d). Their diameter is distributed in the range of 150–180 nm and the average thickness of the shell is about 50 nm. Figure 1e corresponds to the TEM image of ZC1, showing that the NWs are sheathed uniformly with a 10 nm-thick CdS outerlayer. They were rotated on the grid to show that their diameter remained virtually unchanged. The (001) planes of the single-crystalline wurtzite CdS crystal is well aligned with the (001) planes of ZnO (Figure 1f). The CdS (002) fringes are separated by a distance of about 3.3 Å, which is slightly lower than that of the bulk CdS (JCPDS Card No. 41-1049; $a = 4.14092$ Å, $c = 6.7198$ Å). The fast Fourier-Transform (FFT) ED pattern (zone axis = [2110]), generated from the inversion of the TEM image using Digital Micrograph GMS1.4 software (Gatan, Inc.), reveals 7° tilt angle between the CdS [0001] and ZnO [0001] directions, with a number of defective planes at the interfaces (insets). In the ZC2, the outer region of the 50 nm-thick shell exhibits a more polycrystalline nature, as shown in the Supporting Information (SI), Figure S1. The EDX elemental mapping and line-

scanning profile of ZC1 and ZC2 identify the presence of ZnO in the core part and CdS in the shell part (Figure 1 panels g and h). The scanning TEM (STEM) image is shown in the inset. A significant amount of Zn element is distributed over the shell part. The EDX spectrum analysis identifies the Cd and S elements with $[Cd]:[S] = 1:1$ (SI, Figure S2).

Synthesis of $ZnO-CdS_{0.5}Se_{0.5}$ Core–Shell NCs. We synthesized the NC samples having 50 (± 10) nm-thick $CdS_{0.5}Se_{0.5}$ outerlayers, and referred to them as “ZC3”. Figure 2a shows a TEM image of the typical ZC3. The lattice-resolved image of the interface region reveals a single-crystalline wurtzite shell with the (001) planes parallel to the ZnO (001) planes (Figure 2b). The (001) fringes of the shell part are separated by a distance of about 6.9 Å, respectively, which is close to that of the bulk $CdS_{0.5}Se_{0.5}$ (6.86 Å), calculated using the lattice parameters of the wurtzite CdS and CdSe (JCPDS Card No. 77-2307; $a = 4.299$ Å, $c = 7.010$ Å) and the linear dependence of the lattice constants on the mole ratio (Vegard’s law).⁴¹ The FFT ED pattern (zone axis = $[1\bar{1}0]$) reveals the [0001] direction of CdSSe, aligned to the ZnO [0001] directions (insets). The EDX elemental mapping and line-scanning profile identify the ZnO core and the $CdS_{0.5}Se_{0.5}$ shell (Figure 2 panels c and d). Its STEM image is shown in the inset. The Zn element exists in the shell part, similarly to the case of $ZnO-CdS$ (ZC1 and ZC2). The EDX spectrum analysis identifies the composition to be $[S]/([S] + [Se]) = 0.5 \pm 0.1$ (SI, Figure S2).

Synthesis of $ZnO-CdSe$ Core–Shell NCs. The $ZnO-CdSe$ NC samples having 50 (± 10) nm-thick CdSe outerlayers were synthesized (we referred to them as “ZC4”). Figure 2e corresponds to the TEM image for the ZnO NWs sheathed with the 50 nm-thick CdSe. The lattice-resolved image of the interface region reveals a single-crystalline wurtzite CdSe outerlayer with an [0001] direction along the ZnO NW axis (Figure 2f). The (001) fringes are separated by a distance of about 7.0 Å, which is close to that of the bulk CdSe. The FFT ED pattern (zone axis = $[2\bar{1}\bar{1}0]$) confirms the formation of a single-crystalline wurtzite CdSe shell (inset). The EDX elemental mapping and line-scanning profile identify the ZnO core and the CdSe shell, with a continuous distribution of Zn element over the shell part (Figure 2 panels g and h). The STEM image is shown in the inset. The EDX spectrum shows the composition ratio of $[Cd]/[Se]$ to be 1 ± 0.1 (SI, Figure S2).

Synthesis of TiO_2-CdS Core–Shell NCs. Figure 3a shows a SEM image of the high-density TiO_2 NW array grown over a large area of the Ti substrate. The side view reveals that the NWs grew to a length of ~ 10 μ m. The TEM images reveal that the surface is smooth and the average diameter is 60 ± 10 nm (Figure 3b and top inset). They consist of highly crystalline rutile (tetragonal) TiO_2 nanocrystals grown along the $[110]$ direction. The distance between the (110) planes is about 3.2 Å, which

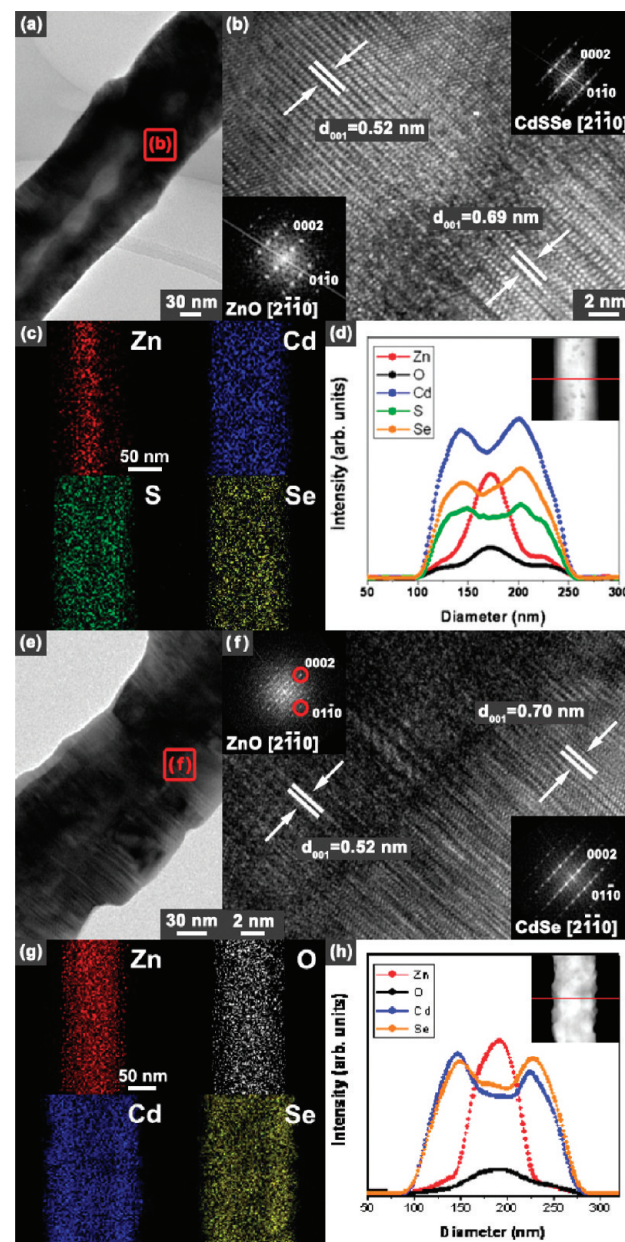


Figure 2. (a) TEM images showing the $ZnO-CdS_{0.5}Se_{0.5}$ (ZC3) having 50 nm-thick shell. (b) The lattice-resolved image of the interface region shows that the [0001] direction of the single-crystalline wurtzite $CdS_{0.5}Se_{0.5}$ is aligned along the wire axis ([0001]) of ZnO. Its corresponding FFT ED pattern confirms the alignment of the [0001] direction of the CdSSe and ZnO (insets). EDX elemental (c) mapping and (d) line-scan reveal the presence of Zn and O elements in the core part, and Cd, S, and Se elements in the shell part with a composition ratio of $[S]/([S] + [Se]) = 0.5$. (e) TEM image showing the $ZnO-CdSe$ (ZC4) having 50 nm-thick shell. (f) Lattice-resolved image showing the aligned [0001] direction of the single-crystalline wurtzite CdSe along the [0001] wire axis of ZnO. Its corresponding FFT ED pattern confirms the alignment of the [0001] direction of the CdS and ZnO (insets). EDX elemental (g) mapping and (h) line-scan reveal the presence of Zn and O elements in the core part and Cd and Se element in the shell part.

is consistent with that of rutile TiO_2 (JCPDS Card No. 86-0147; $a = 4.594$ Å, $c = 2.958$ Å). The bottom inset shows the corresponding FFT ED pattern. All of the nanowires we observed had the same growth direction.

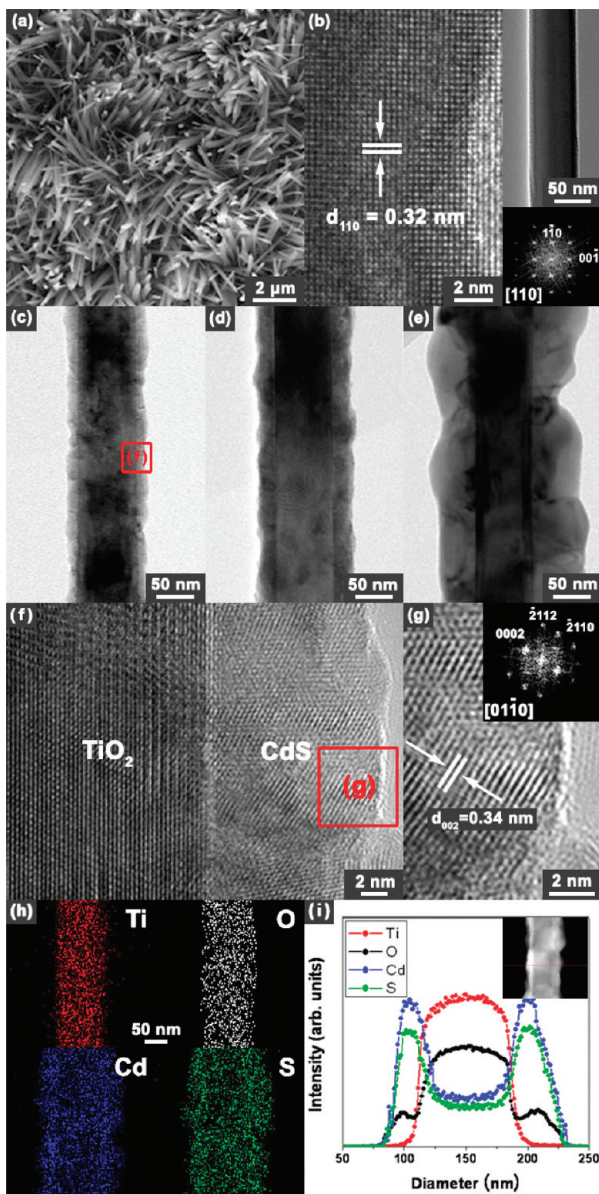


Figure 3. (a) SEM micrograph of the high-density vertically aligned TiO_2 NW array on the large-area Ti substrate. (b) Lattice-resolved TEM images of a selected NW (whose large-scale image is shown in the top inset) and its corresponding FFT ED pattern (bottom inset), revealing the single-crystalline rutile TiO_2 nanocrystals grown along the $[110]$ direction. The TEM images reveal the TiO_2 –CdS coaxial NC structure with (c) 10 nm- (TC1), (d) 20 nm- (TC2), and (e) 50 nm-thick (TC3) CdS shells. (f) Lattice-resolved image of the interface region of the TiO_2 core and CdS shell (TC1), and (g) magnified image of the single-crystalline CdS nanocrystal domain and its corresponding FFT ED pattern (inset). (h) EDX elemental mapping and (i) line-scan over the cross-section of TC2, revealing the presence of Ti and O elements in the core part and Cd and S elements in the shell part. The STEM image is shown in the inset.

We synthesized the TiO_2 –CdS NC samples having 10 ± 5 , 20 ± 10 , and 50 ± 10 nm-thick CdS shells, as “TC1”, “TC2”, and “TC3”, respectively. Figure 3c shows a TEM image of the TiO_2 –CdS core–shell NCs. The CdS layers are coated along the entire length of the straight TiO_2 NWs. Their outer diameter is 70 nm and the thick-

ness of the outerlayers is about 10 nm. Figure 3 panels d and e correspond to the TEM images for the TiO_2 NWs sheathed with the 20 nm- and 50-nm thick CdS outerlayers, respectively. The lattice-resolved image of the interface region reveals that the highly crystalline TiO_2 NW core is covered by a polycrystalline CdS shell that contains a number of single-crystalline domains with no preferential alignment along the wire axis (Figure 3f). Figure 3g shows that the CdS (002) fringes are separated by a distance of about 3.4 Å, which is close to that of the bulk. The FFT ED pattern (zone axis = $[01\bar{1}0]$) confirms the formation of a single-crystalline domain with a size of 10–15 nm (inset).

The EDX elemental mapping of TC2 reveals that the outerlayers are homogeneously composed of Cd and S elements (Figure 3h). The EDX line scanning identifies the presence of Ti and O elements in the core part and Cd and S elements in the shell part (Figure 3i). It is noteworthy that the O composition resides in the CdS shell, which is related to the defects of the polycrystalline phase, as discussed later. The STEM image is shown in the inset. The EDX analysis identifies the presence of Cd and S with an atomic ratio of nearly 1:1 (SI, Figure S2).

XRD Pattern. Figure 4a shows the XRD pattern of the ZnO NWs, ZC1–ZC4. The dominant (002) peak of the ZnO NWs is due to the vertical alignment of the $[0001]$ growth direction. The CdS (002) peak of the ZC1 (10 nm-thick) is strongly enhanced, because of the alignment of the $[0001]$ direction along the $[0001]$ growth direction of the ZnO NW core. For the ZC2–ZC4 samples (50 nm thick shell), the intensity of the (100) and (101) peaks is increased due to the lesser alignment of the CdS (001) planes in the outer region of the shell (as discussed above). The magnified-scaled ZnO (002) peak shows nearly the same width for all four samples, indicating that the lattice constant distortion is negligible in the interface region (Figure 4b). However, these NC samples show a peak shift to a higher angle, up to of $\Delta(2\theta) = 0.1$ degrees (ZC3). Figure 4c corresponds to the magnified-scaled CdSSe (002) peak along with that of the CdS and CdSe NWs. A large amount of broadening with the significant peak shift to a higher angle can be observed for the ZC1 (10 nm thick CdS). When the shell thickness is 50 nm (ZC2), the peak shifts becomes negligible from that of the CdS NWs, with less broadening. The peak position of the ZC3 and ZC4 is consistent with that of the $\text{CdS}_{0.5}\text{Se}_{0.5}$ and CdSe, respectively. The peak broadening of the ZC3 would be related with the assorted distribution of Cd–S–Se ternary composition.

The XRD patterns of the TiO_2 NWs and the three NC samples (TC1–TC3), confirming the growth of the wurtzite CdS shell with a controlled thickness (Figure 4d). The broader peak TiO_2 (110) peaks width compared with that of the TiO_2 NWs indicates that the lattice con-

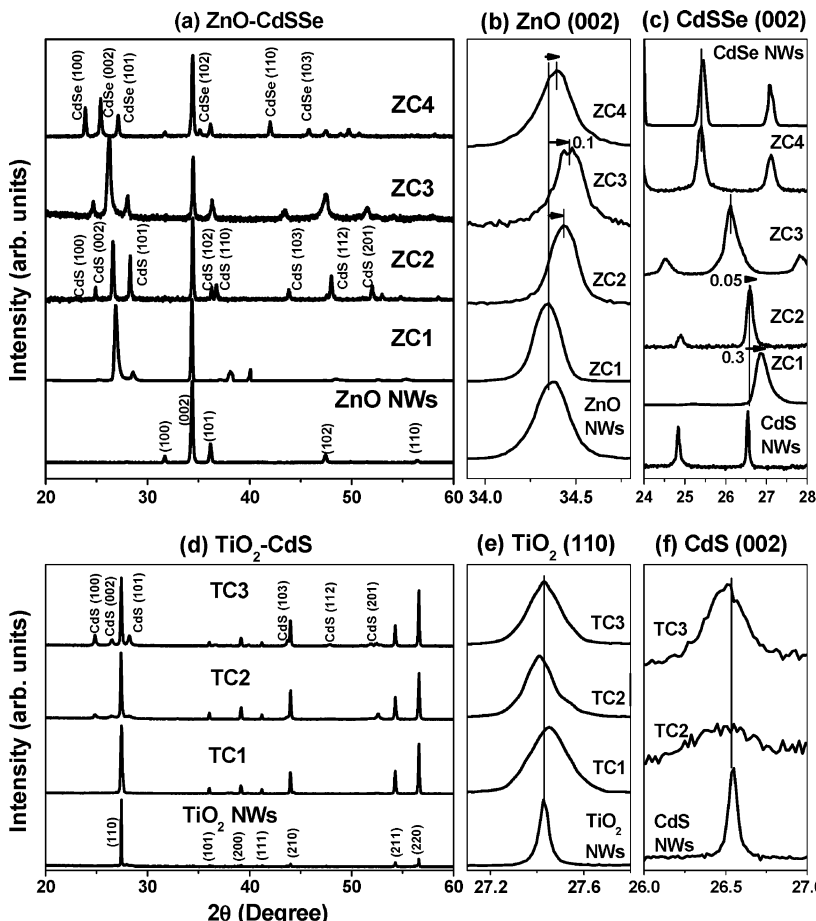


Figure 4. XRD patterns of the (a) ZnO NWs and four ZnO–CdSSe NCs (ZC1–ZC4). Magnified-scaled of the (b) ZnO (002) and (c) CdSSe (002) peaks, with that of the CdS and CdSe NWs. XRD patterns of the (d) TiO₂ NWs, and three TiO₂–CdS NCs (TC1–TC3). Magnified-scaled of the (e) TiO₂ (110) and (f) CdS (002) peaks, with that of the CdS NWs.

stants are probably distorted in the TiO₂–CdS interface region (Figure 4e). The TC2 and TC3 samples exhibit a broader CdS (002) peak width, relative to that of the CdS NWs, which is ascribed to their polycrystalline nature (Figure 4f). The average value of lattice constants (of both ZnO and CdS) remains nearly the same upon the deposition of the CdS outerlayers.

For ZC1 (thickness = 10 nm), the significant shift of the CdS peak to a higher angle is attributed to the heavy doping of the Zn element; the substitution of the Cd²⁺ ions ($r(\text{Cd}^{2+}) = 0.92 \text{ \AA}$) with the smaller radius Zn²⁺ ions ($r(\text{Zn}^{2+}) = 0.74 \text{ \AA}$) contracts the lattice constants of CdS. The value of $\Delta(2\theta) = 0.3^\circ$ implies that there is a 1.2% contraction of the lattice constant c . The corresponding composition is estimated to be Cd_{0.83}Zn_{0.17}S, using the lattice parameters of wurtzite ZnS crystal (JCPDS Card No. 36-1450; $a = 3.82098 \text{ \AA}$, $c = 6.2573 \text{ \AA}$).^{42,43} The large peak broadening suggests a wide composition range along the radial direction. The maximum value of $\Delta(2\theta) = 1.15$ degrees corresponds to a composition of Cd_{0.4}Zn_{0.6}S. As the shell thickness increases to 50 nm (ZC2), the Zn composition decreases to $\sim 1\%$ (Cd_{0.99}Zn_{0.01}S). This result may be directly correlated

with the lower concentration at the furthest position from the core–shell interface (as shown in the EDX data), since the XRD pattern comes mainly from the surface region.

The growth of the shell on the ZnO NW surface may induce compressive strains toward the ZnO NW core, thereby decreasing the lattice constant of the core, for example, 0.2% for ZC2. It should be emphasized that the formation of Zn-containing alloy can reduce the lattice mismatch between the ZnO core and CdSSe shell; *cf.* $c = 5.02661 \text{ \AA}$ (ZnO), 6.7198 \AA (CdS), 6.2573 \AA (ZnS), 7.010 \AA (CdSe), 6.506 \AA (ZnSe). Therefore, the introduction of the CdZnSSe intermediate layer can lead to a reduction in the number of interfacial defects and facilitate the growth of single-crystalline layers on the surface of ZnO. Nevertheless, the small tilt angle between the CdSSe and ZnO [0001] directions appears inevitably due to the lattice mismatch. In contrast, the TiO₂–CdS (TC1–TC3) shows negligible contraction or expansion of average lattice constant, indicating that there is no alloy formation, in contrast to the ZnO–CdSSe NCs. The polycrystalline CdS shell may produce much lower compressive strains toward the TiO₂ NW core.

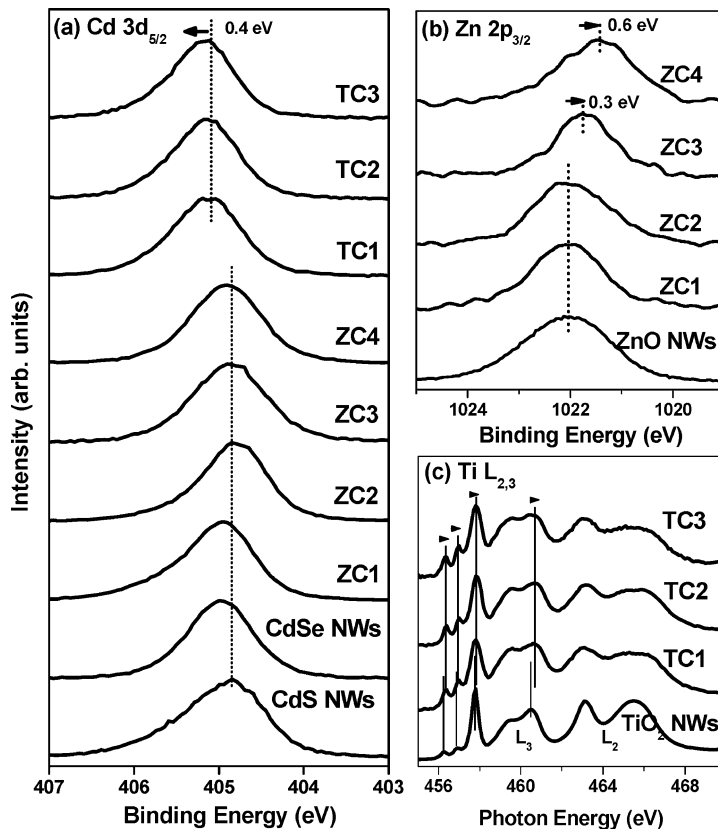


Figure 5. (a) Fine-scanned XPS Cd 3d_{5/2} peak of CdS, CdSe NWs, and seven NC samples. (b) Fine-scanned XPS Zn 2p_{3/2} peak of ZnO NWs and ZnO–CdSSe NCs (ZC1–ZC4). (c) Ti L_{2,3}-edge NEXAFS peak of TiO₂ NWs and TiO₂–CdS NCs (TC1–TC3).

XPS and NEXAFS. Survey-scanned XPS spectrum of the NC samples, and ZnO and TiO₂ NWs is shown in SI, Figure S3. Figure 5a shows fine-scanned XPS Cd 3d_{5/2} peaks of CdS and CdSe NWs and seven (ZC1–ZC4, TC1–TC3) NC samples. The ZnO–CdSSe shows nearly the same binding energy as that of the CdS or CdSe NWs. However, the binding energy of the TiO₂–CdS is increased by 0.4 eV, which could be due to the presence of oxygen atoms in the shell (as shown in Figure 3i). Figure 5b corresponds to fine-scanned Zn 2p_{3/2} peaks of the ZnO NWs and ZnO–CdSSe NCs (ZC1–ZC4). For ZC1 and ZC2, there is no change in the binding energy upon the deposition of the CdS outerlayers. As the Se content increases, the peak shifts to the lower energy (0.3 eV for ZC3 and 0.6 eV for ZC4), probably due to its lower electronegativity than that of the S element. Figure 5c shows Ti L_{2,3}-edge NEXAFS spectra of TiO₂ NWs and TiO₂–CdS NCs (TC1–TC3). Since the XPS of these samples shows no Ti peaks, the NEXAFS spectrum was measured instead. As the CdS outerlayer deposits, the Ti peak shifts slightly to the higher energy by 0.1 eV, and its width becomes broader, indicating the increase in the number of O (oxygen)-related defect sites in the interface region.

These XPS and NEXAFS data support the view that the ZnO–CdSSe NCs have a fewer number of oxygen defect sites at the core–shell interface, than the

TiO₂–CdS NCs. The ZnO NWs were synthesized at 500 °C, while the TiO₂ NWs were synthesized at 800 °C. It is expected that the epitaxial growth of the CdSSe layers at 600 °C would easily form CdZnSSe phase by melting the ZnO NW surface, which can protect the oxygen incorporation during the shell growth.

UV–Visible Absorption and PL Spectra. Figure 6a shows the UV–visible absorption spectra of the ZnO, CdS, and CdSe NWs and NC samples. The band gaps of the ZnO NWs were estimated to be 3.15 eV from the onset of the absorption curves (as marked by the dotted lines), which is close to the bulk value, 3.2 eV. The band gap of the CdS and CdSe NWs is estimated as 2.35 and 1.66 eV, which are consistent with the bulk values: 2.4 and 1.7 eV at room temperature, respectively. The band gap of ZC1 is observed at 2.48 eV, which is blue-shifted from that of the CdS NWs. The ZC2 exhibit a red shift (2.35 eV) upon the increase of shell thickness, which approaches to a value of the CdS NWs. The ZC3 exhibit a band gap at 1.95 eV, matching well to that of the bulk CdS_{0.5}Se_{0.5}.⁴¹ The band gap of ZC4 appears as 1.66 eV, which is the same as that of CdSe NWs. The band gaps of the TiO₂ NWs were estimated to be 3.04 eV from the onset of the absorption curves, which are close to the bulk values, 3.0 eV (rutile TiO₂). The band gap of TC1 appears at 2.34 eV, which is red-shifted from that of the CdS NWs. The red shift becomes more significant with

increasing CdS shell growth; 2.29 eV for TC2 and 2.24 eV for TC3.

Figure 6b shows the PL spectra of the ZnO, CdS, and CdSe NWs, and the NC samples (ZC1–ZC4, TC2, and TC3), recorded at 8 K, by 325 nm He–Cd laser excitation. The CdS and CdSe NWs exhibit a band-edge emission peak at 2.53 and 1.73 eV, respectively. In the case of the ZnO–CdS NCs, the band-edge emission peak appears at 2.63 eV for ZC1, 2.56 eV for ZC2, showing a higher band gap than that of the CdS NWs, which is consistent with the absorption spectrum. The band gap decreased with increasing shell thickness, but is still higher than that of the CdS NWs. Weak defect peaks appear in the higher energy region (2.15 eV). The ZC3 and ZC4 show a band edge emission at 2.13 and 1.73 eV, consistently with that of the bulk CdS_{0.5}Se_{0.5} and CdSe NW, respectively. For TiO₂–CdS NCs, the thicker CdS shell causes the red shift of the band-edge emission: 2.53 eV for TC2 and 2.49 eV for TC3. The broad emission band centered at 2.1 eV is thought to originate from the defect sites formed at the TiO₂–CdS interface, since its intensity relative to that of the band-edge emission decreases with increasing thickness of the shell.

Figure 6c shows the room-temperature PL decay curve of the CdS NWs, ZC2, and TC3, measured at 2.48 eV (500 nm), using 3.1 eV (400 nm) frequency-doubled Ti–sapphire laser pulses as the excitation source. The decay time of TC3 appears to be nearly the same as that of the CdS NWs, but that of ZC2 is significantly reduced. Their steady-state PL spectra show that the band-edge emissions appear at 2.43, 2.47, and 2.44 eV, respectively, for the CdS NWs, ZC2, and TC3 (inset). The experimental curves were fitted with one or two exponential decay response functions. The best fitted parameters, α_i (amplitude) and τ_i (decay time), are shown in Table 1. The average decay time $\langle\tau\rangle$ was calculated using the equation, $\langle\tau\rangle = (\alpha_1\tau_1^2 + \alpha_2\tau_2^2)/(\alpha_1\tau_1 + \alpha_2\tau_2)$. The $\langle\tau\rangle$ value is 0.92, 0.093, and 0.95 ns for the CdS NWs, ZC2, and TC3, respectively.

For the TiO₂–CdS NCs, as the thickness of the CdS shell increases, the absorption and PL spectra exhibit a red shift. Our result is consistent with previous works on ZnO–CdS, TiO₂–CdS, and TiO₂–CdSe composite nanostructures.^{17,18,21,44–49} This behavior is typical of type-II core–shell nanostructures that exhibit a new absorption feature due to weakly “spatially indirect” transitions with energies that are lower than the pure CdS band gap.^{50,51} The TiO₂ and CdS provide for light collection and photoinduced charge transfer, respectively. The photoexcited electrons and holes reside in the different semiconductor; therefore, the energy gradient existing at the interface tends to spatially separate the electrons and holes. The corresponding “spatially indirect” energy gap is determined by the energy separation between the CB edge of TiO₂ and the VB edge of CdS. The band gap of CdS can depend on the shell

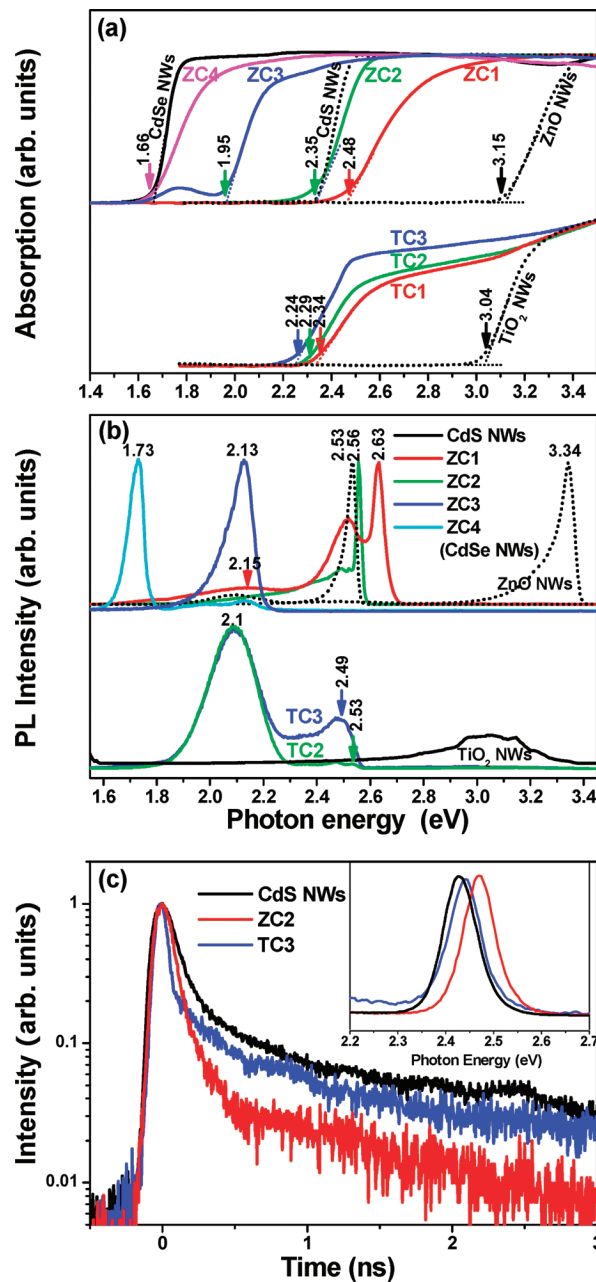


Figure 6. (a) UV–visible absorption spectra of the TiO₂, ZnO, CdS, and CdSe NWs (ZC1–ZC4), and TiO₂–CdS (ZC1–ZC3). (b) PL spectra of the TiO₂, ZnO, CdS, and CdSe NW, and ZnO–CdSSe (ZC1–ZC4), and TiO₂–CdS (TC1–TC3), measured at 8 K. The excitation source is a He–Cd laser ($\lambda = 325$ nm). (c) Time-resolved PL spectra of the CdS NWs, ZC2, and TC3, at room temperature, and their steady-state spectra (inset), obtained using a frequency-doubled Ti–sapphire laser ($\lambda = 400$ nm) as the excitation source.

TABLE 1. Fitting Parameters of TCSPC Data Measured from ZnO–CdS (ZC2) and TiO₂–CdS (TC3) Core–Shell NC Arrays

sample name	core	α_1	τ_1 (ns)	α_2	τ_2 (ns)	$\langle\tau\rangle$ (ns)
CdS		0.94	0.107	0.06	1.72	0.92
ZC2	ZnO	1	0.09			0.093
TC3	TiO ₂	0.69	0.15	0.31	1.18	0.95

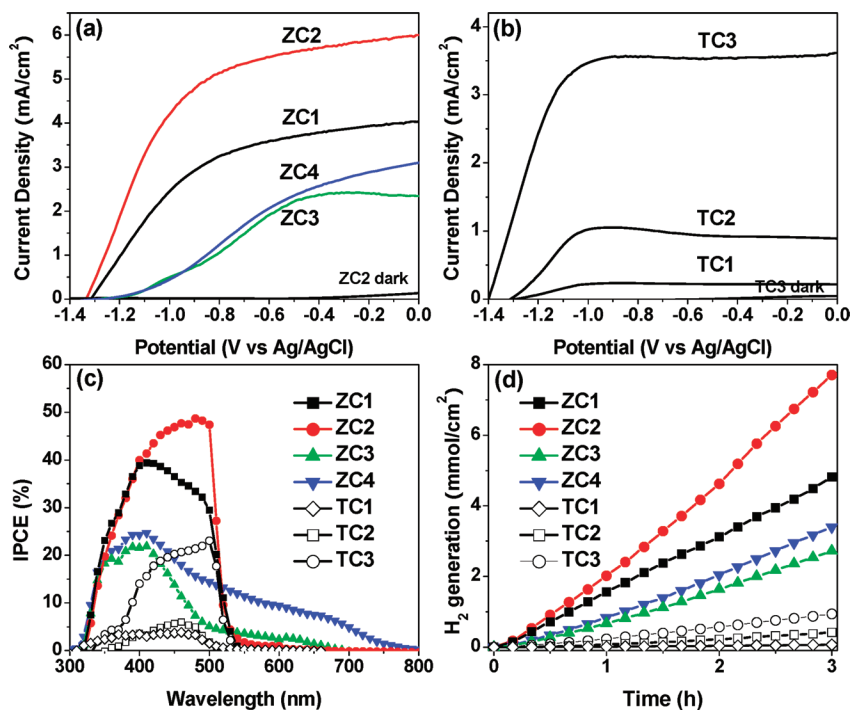


Figure 7. Photocurrent density (mA/cm^2) vs potential (V vs Ag/AgCl) for (a) $\text{ZnO}-\text{CdSSe}$ (ZC1~ZC4), and (b) TiO_2-CdS (TC1~TC3) NC samples, measured under visible light illumination ($100 \text{ mW}/\text{cm}^2$) in a $1 \text{ M Na}_2\text{S}$ solution. (c) Measured IPCE spectra of $\text{ZnO}-\text{CdSSe}$ (ZC1~ZC4) and TiO_2-CdS (TC1~TC3), collected at the incident wavelength range from 300 – 800 nm , at potential of 0 V vs Ag/AgCl . (d) Time-dependent H_2 evolution (mmol/cm^2) in the PEC using the NC samples (ZC1~ZC4 and TC1~TC3) as the photoanodes.

thickness due to the greater number of defect sites of the polycrystalline layers. With increasing shell thickness, the band gap of CdS decreases and consequently lowers the CB offset value. This smaller CB offset is responsible for the red shift of the absorption and emission bands. The slightly longer excited-state lifetime of TC3 than that of the CdS NWs also supports the existence of such charge-separated states.

In the case of the $\text{ZnO}-\text{CdS}$ NCs, the larger band gap must be due to the formation of CdZnS alloy. As the thickness of the CdS shell increases, the Zn concentration decreases along the outward direction (as discussed in relation to the EDX and XRD data) and, thus, the band gap can decrease. From the blue shifts of their PL emissions, 0.1 eV (ZC1) and 0.03 eV (ZC2), the compositions of ZC1 and ZC2 were estimated to be

$\text{Cd}_{0.85}\text{Zn}_{0.15}\text{S}$ and $\text{Cd}_{0.98}\text{Zn}_{0.02}\text{S}$, respectively, which are consistent with the XRD data. The shorter excited-state lifetime of ZC2 than that of TC3 is ascribed to the larger band gap and CB band offset of the CdZnS alloy layers; a larger band gap usually results in a shorter excited-state lifetime. The single-crystalline nature along with the alignment of the CdZnSSe [0001] direction along the ZnO [0001] direction and the lesser number of defects in the interface region would contribute to the efficient production of charge-separated states that would make the NCs more suitable for PEC or photovoltaic applications, as described in the following data.

Photoelectrochemical Cell. Figure 7a shows the photocurrent density J (mA/cm^2) vs applied potential V (vs Ag/AgCl) curves of the PECs, using ZC1~ZC4 as the photo-

TABLE 2. Performance Parameters of PECs Based on $\text{ZnO}-\text{CdSSe}$ and TiO_2-CdS Core–Shell NC Arrays with CdS Shells Having Different Thicknesses, Measured under Visible Light Illumination ($100 \text{ mW}/\text{cm}^2$, AM 1.5G)

sample name	core	shell	shell thickness (nm)	J (mA/cm^2)	V (V)	H_2 generation rate ($\text{mmol}/\text{cm}^2\text{hW}$)
ZC1	ZnO	CdS	10	4.0	1.3	16
ZC2		CdS	50	6.0	1.3	26
ZC3		$\text{CdS}_{0.5}\text{Se}_{0.5}$	50	2.4	1.2	8.3
ZC4		CdSe	50	3.1	1.2	11
TC1	TiO_2	CdS	10	0.22	1.3	0.21
TC2		CdS	20	0.90	1.3	1.4
TC3		CdS	50	3.6	1.4	3.2

anodes, in 1 M Na_2S electrolyte under Xe light illumination of 100 mW/cm^2 (AM 1.5G). The dark current is very low (10^{-7} A/cm^2) for all of the samples. The photocurrent density (J) increases with increasing thickness of the CdS outerlayer, that is, $J = 4.0, 6.0, 2.4$, and 3.1 mA/cm^2 for ZC1–ZC4, respectively. Table 2 lists the J and V (onset potential) values of the PECs. Figure 7b corresponds to the J – V characterization curve, measured using the TC1–TC3 photoanodes, showing the increase in the photocurrent with increasing thickness of the CdS shell, that is, 0.22, 0.90, and 3.6 mA/cm^2 for TC1–TC3, respectively. The photocurrent response data shows a fast response/recovery time with good reproducibility (SI, Figure S4).

We performed incident-photon-to-current-conversion efficiency (IPCE) measurements to study their photoresponse as a function of incident light wavelength (Figure 7c). The IPCE at different wavelengths is determined from the short circuit photocurrents (I_{sc}) monitored at different excitation wavelengths (λ) to compare the photoresponse of the samples using an equation, $\text{IPCE} (\%) = [1240 \times I_{sc} (\text{mA/cm}^2)] / [\lambda (\text{nm})/I_{in} (\text{W/cm}^2)] \times 100$, where I_{in} is the incident light power. The ZnO– and TiO_2 –CdS (ZC1, ZC2, TC1–TC3) samples had a pronounced IPCE at the wavelength up to 500 nm and then the IPCE dropped to a minimal level at a wavelength below the CdS band gap energy of 530 nm. A maximum IPCE of 40% is achieved for the ZC1 electrode. Under the same conditions, the maximum IPCE values of 49% for ZC2 and 23% for TC3 are observed. On the other hand, the ZnO–CdSSe (ZC3) and –CdSe– (ZC4) samples showed photoactivity at a broader range of wavelength to 700 and 800 nm, respectively, due to their smaller band gap, with a maximum IPCE value of 22 and 25%.

Figure 7d shows a quantitative description of the H_2 evolution as a function of time for a PEC with a Pt cathode and the NC photoanode, in 1 M Na_2S electrolyte under Xe light illumination of 100 mW/cm^2 (AM 1.5G). During 3 h exposure, 4.8, 7.7, 2.5, and 3.4 mmol/cm^2 of H_2 were generated for ZC1–ZC4, respectively, corresponding to rates of 16, 26, 8.3, and $11 \text{ mmol/(cm}^2 \text{ h W)}$. TC1–TC3 exhibited rates of 0.64, 4.1, and 9.5 mmol/cm^2 , corresponding to 0.21, 1.4, and $3.2 \text{ mmol/(cm}^2 \text{ h W)}$, respectively, which are lower than the values obtained for the ZnO–CdS NCs.

The architecture of the core–shell NCs, in this case the thickness of the CdS shell, has a significant effect on the efficiency of the PEC. A CdS shell with a larger thickness allows for more efficient absorption of the incident photons, as well as decreasing the recombination rate of electron–hole pairs (as discussed above), which results in larger photocurrents. We can also explain the present result by referring to the model of Lubberhuizen *et al.* proposed for nanoporous GaP.⁵² The photogenerated charge carriers are instantaneously and effectively

separated by the capture of holes in the surface bonds. The recombination between the separated electrons and holes is sensitive to the band-bending potential that the electrons have to overcome to reach the surface where recombination takes place. Therefore, the greater the band-bending potential, the smaller the amount of charge carrier recombination. As a consequence, we would anticipate greater band bending from the thicker CdS shell, thus decreasing the surface recombination rates and consequently enhancing the photocurrent. Unfortunately, the growth of the shell being thicker than 50 nm was not successful under our growth condition. The finding of the optimum thickness to guarantee the highest PEC efficiency remains as a future work.

The higher PEC efficiency of the ZnO–CdS NCs, as compared to that of the TiO_2 –CdS, is attributed to the formation of CdZnS alloy, as discussed above. The less lattice mismatch between the shell and core would result in a more single-crystalline defect-free shell, which enhances the quantum yield for the photogeneration of charge carriers. It also decreases the carrier loss in the interface region and, thus, increases the charge separation efficiency as well. In addition, ZnO has a higher carrier mobility than TiO_2 ; 0.2 – $10 \text{ cm}^2/(\text{V} \cdot \text{s})$ for rutile TiO_2 and $205 \text{ cm}^2/(\text{V} \cdot \text{s})$ for ZnO, which also contributes to facilitating the charge separation.^{53–55} The photocurrents, IPCE, and H_2 generation rate showed consistently that the ZnO–CdS was more efficient than the ZnO–CdSe in separating and/or collecting photoexcited electrons, which is in agreement with the larger potential difference between the conduction band of CdS and ZnO.¹⁹ The PEC efficiency of the ZnO– $\text{CdS}_{0.5}\text{Se}_{0.5}$ is rather close to that of the ZnO–CdSe. To understand this result, we presently study the PEC properties of the finely tuned composition shelled ZnO and TiO_2 NW arrays.

CONCLUSIONS

We synthesized high-density ZnO–CdSSe core–shell NC arrays by depositing CdS outerlayers on pregrown vertically aligned ZnO (wurtzite) NW arrays using the CVD method. The composition was tuned from CdS to CdSe via $\text{CdS}_{0.5}\text{Se}_{0.5}$, and the thickness of the CdS shell was controlled to be 10–50 nm by adjusting the growth conditions. The shell consisted of single-crystalline wurtzite nanocrystals whose [0001] direction was aligned along the wire axis [0001] of the ZnO NWs. However, the CdS shell of the TiO_2 –CdS NCs, grown under the same growth condition, consisted of a number of single-crystalline domains randomly aligned along the wire axis. For the ZnO–CdSSe NCs, the XRD, XPS, NEXAFS, UV–visible absorption, and PL data confirmed the formation of Zn containing alloy layers in the interface region, which can facilitate the epitaxial growth of single-crystalline shell layers on the ZnO NW core, by reducing both the lattice mismatch

and the number of defect sites. We fabricated PECs using these arrays as the photoanode and measured their photocurrents, as well as the rate of H_2 generation under AM 1.5G conditions. A thicker shell results in better performance of the PEC; the photocurrents of $ZnO-CdS$ (ZC2) and TiO_2-CdS (TC3) with 50 nm thick

shells were 6.2 and 3.5 mA/cm^2 , respectively. The respective H_2 generation rates were 26 and 3.2 $mmol/(cm^2 h W)$. We suggest that the formation of the Zn-containing alloy layers contributes to the higher PEC performance of the $ZnO-CdSSe$ NCs, by enhancing the charge separation.

EXPERIMENTAL SECTION

For the synthesis of the ZnO NW array, Zn powder (99.99%, Aldrich) was used to generate Zn vapor, and a piece of ultrasonically cleaned Ti or Ni foil ($10 \times 10 \times 0.25 mm^3$) with a purity of 99.7% (Aldrich) was used as a substrate. The Zn powder was placed in a quartz boat, located inside a quartz tube reactor, and the substrate was on the top of this boat. An argon flow at 200 sccm was introduced into the reactor tube, followed by heating to 500 °C. The growth reaction was maintained for 60 min. To synthesize the TiO_2 NW array, the Ti foils were used as both the Ti source and substrates. A flow of oxygen (>99.999%) with a rate of 20–50 sccm was introduced only for the reaction time of 60 min, and then the Ti foils were covered homogeneously with the white-colored NW array.

To deposit the CdSSe outerlayers, the ZnO or TiO_2 NWs (grown on the substrates) were placed a few cm apart from CdS (99.995%, Aldrich) or CdSe (99.99%, Aldrich), CdS/CdSe mixed powder, inside the reactor. As the CdS/CdSe powder was evaporated at 850 °C for 10–60 min under argon flow, the CdSSe layers were deposited on the NW array at about 600 °C. The thickness of the CdSSe shell was controlled by adjusting the growth temperature or time. The composition was controlled by changing the ratio of CdS and CdSe powders. We also synthesized CdS and CdSe NWs using 3 nm-thick Au film-deposited Si substrates, under the same growth conditions, as described elsewhere.⁴⁰

The products were analyzed by scanning electron microscopy (SEM, Hitachi S-4700), field-emission transmission electron microscopy (TEM, Jeol JEM 2100F and FEI TECNAI G² 200 kV), high-voltage TEM (HVEM, Jeol JEM ARM 1300S, 1.25 MV), and energy-dispersive X-ray fluorescence spectroscopy (EDX). High-resolution X-ray diffraction (XRD) patterns were obtained using the 8C2 and 3C2 beamlines of the Pohang Light Source (PLS) with monochromatic radiation ($\lambda = 1.54595 \text{ \AA}$). X-ray photoelectron spectroscopy (XPS) was performed using the 8A1 beamline of the PLS and a laboratory-based spectrometer (ESCALAB 250, VG Scientifics) using a photon energy of 1486.6 eV (Al $K\alpha$). Near-edge X-ray absorption fine structure (NEXAFS) measurements were performed at the U7 beamline of PLS. A UV–visible–NIR absorption spectrometer (Varian, Cary 1000) was used to measure the band gap. The temperature-dependent photoluminescence (PL) measurements were carried out using a He–Cd laser ($\lambda = 325 \text{ nm}$) as the excitation source.

The time-resolved PL spectrum was measured using a time-correlated single-photon counting (TCSPC) system, which consisted of a self-mode-locked cavity-dumped Ti–sapphire laser (Mira900, Coherent) pumped by a continuous wave Nd:YAG laser (Coherent, Verdi), with a pulse width of about 150 fs and a repetition rate of 76 MHz. The excitation wavelength was 400 nm, produced by second harmonic generation (SHG). The fluorescence was spectrally resolved using a monochromator (SP-2150i, Acton), and its time-resolved signal was measured by a TCSPC module (PicoHarp, PicoQuant) with an MCP-PMT (R3809U, Hamamatsu). The total instrument response function (IRF) was less than 100 ps, which gives a temporal resolution of less than 10 ps. The deconvolution of the decay curve, which separates the IRF and actual decay signal, was performed using fitting software (FluoFit, PicoQuant) to deduce the time constant associated with each exponential decay. The PL decays were usually analyzed by the multiexponential model: $\exp(-t/\tau_i)$.

The PEC properties of the TiO_2-CdS and $ZnO-CdS$ NC array electrodes were measured as follows. The whole setup consists of a liquid junction PEC. The photocurrent *versus* voltage of the cell was measured with a NC array electrode having a sur-

face area of 0.25 cm^2 . A constant light intensity of 100 mW/cm^2 from a 450 W Xe lamp (Oriel) passed through an AM 1.5G filter was used as the light source. The incident light intensity was calibrated by a standard crystalline silicon solar cell. An electrochemical analyzer (IVIUM, Compactstat) was used to measure the PEC response, with a conventional three-electrode system comprising an Ag/AgCl reference electrode, a Pt foil counterelectrode, and the sample electrode. A 1 M Na_2S aqueous solution was used as the electrolyte. Argon was bubbled through to remove the dissolved oxygen during the measurement. The incident photon-to-current measurement efficiency (IPCE) spectra were measured on an IPCE measurement system (PV Measurement, Inc.). The H_2 evolution as a function of time was monitored by gas chromatography (GC), and its quantity was calibrated using a standard H_2/He gas mixture.

Acknowledgment. This study was supported by NRF (R01-2008-000-10825-0; 2008-02364), and MKE under the auspices of the ITRC support program supervised by the IITA (2008-C1090-0804-0013). This research was also supported by the WCU program through the NRF funded by the Ministry of Education, Science and Technology (R31-10035). The HVEM (Daejeon), XRD (Taegu), and XPS (Pusan) measurements were performed at the KBSI. The experiments at the PLS were partially supported by MOST and POSTECH.

Supporting Information Available: The TEM, EDX, XPS, and $J-t$ data of the PEC. This material is available free of charge via the Internet at <http://pubs.acs.org>.

REFERENCES AND NOTES

1. Fujishima, A.; Honda, K. Electrochemical Photolysis of Water at a Semiconductor Electrode. *Nature* **1972**, *238*, 37–38.
2. Law, M.; Greene, L. E.; Johnson, J. C.; Saykally, R.; Yang, P. Nanowire Dye-Sensitized Solar Cells. *Nat. Mater.* **2005**, *4*, 455–459.
3. Mor, G. K.; Shankar, K.; Paulose, M.; Varghese, O. K.; Grimes, C. A. Use of Highly-Ordered TiO_2 Nanotube Arrays in Dye-Sensitized Solar Cells. *Nano Lett.* **2006**, *6*, 215–218.
4. Feng, X.; Shankar, K.; Varghese, O. K.; Paulose, M.; Latempa, T. J.; Grimes, C. A. Vertically Aligned Single Crystal TiO_2 Nanowire Arrays Grown Directly on Transparent Conducting Oxide Coated Glass: Synthesis Details and Applications. *Nano Lett.* **2008**, *8*, 3781–3786.
5. Kuang, D.; Brillet, J.; Chen, P.; Takata, M.; Uchida, S.; Miura, H.; Sumioka, K.; Zakeeruddin, S. M.; Grätzel, M. Application of Highly Ordered TiO_2 Nanotube Arrays in Flexible Dye-Sensitized Solar Cells. *ACS Nano* **2008**, *2*, 1113–1116.
6. Liu, B.; Aydil, E. S. Growth of Oriented Single-Crystalline Rutile TiO_2 Nanorods on Transparent Conducting Substrates for Dye-Sensitized Solar Cells. *J. Am. Chem. Soc.* **2009**, *131*, 3985–3990.
7. Varghese, O. K.; Paulose, M.; Grimes, C. A. Long Vertically Aligned Titania Nanotubes on Transparent Conducting Oxide for Highly Efficient Solar Cells. *Nat. Nanotechnol.* **2009**, *4*, 592–597.
8. Shankar, K.; Basham, J. I.; Allam, N. K.; Varghese, O. K.; Mor, G. K.; Feng, X.; Paulose, M.; Seabold, J. A.; Choi, K.-S.; Grimes, C. A. Recent Advances in the Use of TiO_2 Nanotube and Nanowire Arrays for Oxidative Photoelectrochemistry. *J. Phys. Chem. C* **2009**, *113*, 6327–6359, and references within.

9. Hochbaum, A. I.; Yang, P. Semiconductor Nanowires for Energy Conversion. *Chem. Rev.* **2010**, *110*, 527.
10. Chen, S.; Paulose, M.; Ruan, C.; Mor, G. K.; Varghese, O. K.; Kouzoudis, D.; Grimes, C. A. Electrochemically Synthesized CdS Nanoparticle-Modified TiO₂ Nanotube-Array Photoelectrodes: Preparation, Characterization, and Application to Photoelectrochemical Cells. *J. Photochem. Photobio. A* **2006**, *177*, 177–184.
11. Yin, Y.; Jin, Z.; Hou, F. Enhanced Solar Water-Splitting Efficiency Using Core/Sheath Heterostructure CdS/TiO₂ Nanotube Arrays. *Nanotechnology* **2007**, *18*, 495608.
12. Sun, W. -T.; Yu, Y.; Pan, H. -Y.; Gao, X. -F.; Chen, Q.; Peng, L. -M. CdS Quantum Dots Sensitized TiO₂ Nanotube-Array Photoelectrodes. *J. Am. Chem. Soc.* **2008**, *130*, 1124–1125.
13. Banerjee, S.; Mohapatra, S. K.; Das, P. P.; Misra, M. Synthesis of Coupled Semiconductor by Filling 1D TiO₂ Nanotubes with CdS. *Chem. Mater.* **2008**, *20*, 6784–6791.
14. Zhang, Y. J.; Yan, W.; Wu, Y. P.; Wang, Z. H. Synthesis of TiO₂ Nanotubes Coupled with CdS Nanoparticles and Production of Hydrogen by Photocatalytic Water Decomposition. *Mater. Lett.* **2008**, *62*, 3846–3848.
15. Wang, C. L.; Sun, L.; Yun, H.; Li, J.; Lai, Y. K.; Lin, C. J. Sonoelectrochemical Synthesis of Highly Photoelectrochemically Active TiO₂ Nanotubes by Incorporating CdS Nanoparticles. *Nanotechnology* **2009**, *20*, 295601/1–295601/6.
16. Fang, F.; Zhao, D. X.; Li, B. H.; Zhang, Z. Z.; Zhang, J. Y.; Shen, D. Z. The Enhancement of ZnO Nanowalls Photoconductivity Induced by CdS Nanoparticle Modification. *Appl. Phys. Lett.* **2008**, *93*, 233115.
17. Tak, Y.; Hong, S. J.; Lee, J. S.; Yong, K. Fabrication of ZnO/CdS Core/Shell Nanowire Arrays for Efficient Solar Energy Conversion. *J. Mater. Chem.* **2009**, *19*, 5945–5951.
18. Zhang, Y.; Xie, T.; Jiang, T.; Wei, X.; Pang, S.; Wang, X.; Wang, D. Surface Photovoltage Characterization of a ZnO Nanowire Array/CdS Quantum Dot Heterogeneous Film and Its Application for Photovoltaic Devices. *Nanotechnology* **2009**, *20*, 155707.
19. Wang, G.; Yang, X.; Qian, F.; Zhang, J. Z.; Li, Y. Double-Sided CdS and CdSe Quantum Dot Co-Sensitized ZnO Nanowire Arrays for Photoelectrochemical Hydrogen Generation. *Nano Lett.* **2010**, *10*, 1088–1092.
20. Chong, S. V.; Suresh, N.; Xia, J.; Al-Salim, N.; Idriss, H. TiO₂ Nanobelts/CdSSe Quantum Dots Nanocomposite. *J. Phys. Chem.* **2007**, *111*, 10389–10393.
21. Konganand, A.; Tvrdo, K.; Takechi, K.; Kuno, M.; Kamat, P. V. Quantum Dot Solar Cells. Tuning Photoresponse through Size and Shape Control of CdSe–TiO₂ Architecture. *J. Am. Chem. Soc.* **2008**, *130*, 4007–4015.
22. Zhang, H.; Quan, X.; Chen, S.; Yu, H.; Ma, N. “Mulberry-like” CdSe Nanoclusters Anchored on TiO₂ Nanotube Arrays: A Novel Architecture with Remarkable Photoelectrochemical Performance. *Chem. Mater.* **2009**, *21*, 3090–3095.
23. Lee, J. -C.; Sung, Y. -M.; Kim, T. G.; Choi, H. -J. TiO₂–CdSe Nanowire Arrays Showing Visible-Range Light Absorption. *Appl. Phys. Lett.* **2007**, *91*, 113104.
24. Tena-Zaera, R.; Katty, A.; Bastide, S.; Lévy-Clément, C. Annealing Effects on the Physical Properties of Electrodeposited ZnO/CdSe Core–Shell Nanowire Arrays. *Chem. Mater.* **2007**, *19*, 1626–1632.
25. Leschke, K. S.; Divakar, R.; Basu, J.; Enache-Pommer, E.; Boercker, J. E.; Carter, C. B.; Kortshagen, U. R.; Norris, D. J.; Aydil, E. S. Photosensitization of ZnO Nanowires with CdSe Quantum Dots for Photovoltaic Devices. *Nano Lett.* **2007**, *7*, 1793–1798.
26. Prabakar, K.; Minku, S.; Heeje, K. CdSe Quantum Dots Co-Sensitized TiO₂ Photoelectrodes: Particle Size Dependent Properties. *J. Phys. D: Appl. Phys.* **2010**, *43*, 012002-1–012002-4.
27. Seibold, J. A.; Shankar, K.; Wilke, R. H. T.; Paulose, M.; Varghese, O. K.; Grimes, C. A.; Choi, K. -S. Photoelectrochemical Properties of Heterojunction CdTe/TiO₂ Electrodes Constructed Using Highly Ordered TiO₂ Nanotube Arrays. *Chem. Mater.* **2008**, *20*, 5266–5273.
28. Cao, X.; Chen, P.; Guo, Y. Decoration of Textured ZnO Nanowires Array with CdTe Quantum Dots: Enhanced Light-Trapping Effect and Photogenerated Charge Separation. *J. Phys. Chem. C* **2008**, *112*, 20560–20566.
29. Wang, K.; Chen, J.; Zhou, W.; Zhang, Y.; Yan, Y.; Pern, J.; Mascarenhas, A. Direct Growth of Highly Mismatched Type II ZnO/ZnSe Core/Shell Nanowire Arrays on Transparent Conducting Oxide Substrates for Solar Cell Applications. *Adv. Mater.* **2008**, *20*, 3248–3253.
30. Yuhas, B. D.; Yang, P. Nanowire-Based All-Oxide Solar Cells. *J. Am. Chem. Soc.* **2009**, *131*, 3756–3761.
31. Kuo, K. -T.; Liu, D. -M.; Chen, S. -Y.; Lin, C. -C. Core–Shell CulnS₂/ZnS Quantum Dots Assembled on Short ZnO Nanowires with Enhanced Photoconversion Efficiency. *J. Mater. Chem.* **2009**, *19*, 6780–6788.
32. Kayes, B. M.; Atwater, H. A.; Lewis, N. S. Comparison of the Device Physics Principles of Planar and Radial p–n Junction Nanorod Solar Cells. *J. Appl. Phys.* **2005**, *97*, 114302.
33. Lewis, N. S. Toward Cost-Effective Solar Energy Use. *Science* **2007**, *315*, 798–801.
34. Zhang, Y.; Wang, L. -W.; Mascarenhas, A. “Quantum Coaxial Cables” for Solar Energy Harvesting. *Nano Lett.* **2007**, *7*, 1264–1269.
35. Schrier, J.; Demchenko, D. O.; Wang, L. -W. Optical Properties of ZnO/ZnS and ZnO/ZnTe Heterostructures for Photovoltaic Applications. *Nano Lett.* **2007**, *7*, 2377–2382.
36. Tian, B.; Zheng, X.; Kempa, T. J.; Fang, Y.; Yu, N.; Yu, G.; Huang, J.; Lieber, C. M. Coaxial Silicon Nanowires as Solar Cells and Nanoelectronic Power Sources. *Nature* **2007**, *449*, 885–889.
37. Tian, B.; Kempa, T. J.; Lieber, C. M. Single Nanowire Photovoltaics. *Chem. Soc. Rev.* **2009**, *38*, 16–24.
38. Hwang, Y. J.; Boukai, A.; Yang, P. High Density n-Si/n-TiO₂ Core/Shell Nanowire Arrays with Enhanced Photoactivity. *Nano Lett.* **2009**, *9*, 410–415.
39. Pan, A. L.; Yao, L.; Qin, Y.; Yang, Y.; Kim, D. S.; Yu, R.; Zhou, B.; Werner, P.; Zacharias, M.; Gösele, U. Si–CdSSe Core/Shell Nanowires with Continuously Tunable Light Emission. *Nano Lett.* **2008**, *8*, 3413.
40. Na, C. W.; Han, D. S.; Kim, D. S.; Kang, Y. J.; Lee, J. Y.; Park, J.; Oh, D. K.; Kim, K. S.; Kim, D. Photoluminescence of Cd_{1-x}Mn_xS (x ≤ 0.3) Nanowires. *J. Phys. Chem. B* **2006**, *110*, 6699–6704.
41. Perna, G.; Pagliara, S.; Capozzi, V.; Ambrico, M.; Ligonzio, T. Optical characterization of CdS_xSe_{1-x} films grown on quartz substrate by pulsed laser ablation technique. *Thin Solid Films* **1999**, *349*, 220–224.
42. Padam, G. K.; Malhotra, G. L.; Rao, S. U. M. Studies on Solution-Grown Thin Films of Zn_xCd_{1-x}S. *J. Appl. Phys.* **1988**, *63*, 770–774.
43. Lee, J. -H.; Song, W. -C.; Yi, J. -S.; Yang, K. -J.; Han, W. -D.; Hwang, J. Growth and Properties of the Cd_{1-x}Zn_xS Thin Films for Solar Cell Applications. *Thin Solid Films* **2003**, *431*–432, 349–353.
44. Chang, C. -H.; Lee, Y. -L. Chemical Bath Deposition of CdS Quantum Dots onto Mesoscopic TiO₂ Films for Application in Quantum-Dot-Sensitized Solar Cells. *Appl. Phys. Lett.* **2007**, *91*, 053503.
45. Laramona, G.; Choné, C.; Jacob, A.; Sakakura, D.; Delatouche, B.; Péré, D.; Cieren, X.; Nagino, M.; Bayón, R. Nanostructured Photovoltaic Cell of the Type Titanium Dioxide, Cadmium Sulfide Thin Coating, and Copper Thiocyanate Showing High Quantum Efficiency. *Chem. Mater.* **2006**, *18*, 1688–1696.
46. Das, K.; De, S. K. Optical Properties of the Type-II Core–Shell TiO₂@CdS Nanorods for Photovoltaic Applications. *J. Phys. Chem. C* **2009**, *113*, 3494–3501.
47. Guijarro, N.; Lana-Villarreal, T.; Mora-Seró, I.; Bisquert, J.; Gómez, R. CdSe Quantum Dot-Sensitized TiO₂ Electrodes: Effect of Quantum Dot Coverage and Mode of Attachment. *J. Phys. Chem. C* **2009**, *113*, 4208–4214.
48. Piris, J.; Ferguson, A. J.; Blackburn, J. L.; Norman, A. G.; Rumbles, G.; Selmarthen, D. C.; Kopidakis, N. Efficient Photoinduced Charge Injection from Chemical Bath

Deposited CdS into Mesoporous TiO₂ Probed with Time-Resolved Microwave Conductivity. *J. Phys. Chem. C* **2008**, *112*, 7742–7749.

- 49. Wang, X.; Liu, G.; Chen, Z.-G.; Li, F.; Wang, L.; Lu, G. Q.; Cheng, H.-M. Enhanced Photocatalytic Hydrogen Evolution by Prolonging the Lifetime of Carriers in ZnO/CdS Heterostructures. *Chem. Commun.* **2009**, 3452–3454.
- 50. Kim, S.; Fisher, B.; Eisler, H.-J.; Bawendi, M. Type-II Quantum Dots: CdTe/CdSe(Core/Shell) and CdSe/ZnTe(Core/Shell) Heterostructures. *J. Am. Chem. Soc.* **2003**, *125*, 11466–11467.
- 51. Ivanov, S. A.; Piryatinski, A.; Nanda, J.; Tretiak, S.; Zavadil, K. R.; Wallace, W. O.; Werder, D.; Klimov, V. I. Type-II Core/Shell CdS/ZnSe Nanocrystals: Synthesis, Electronic Structures, and Spectroscopic Properties. *J. Am. Chem. Soc.* **2007**, *129*, 11708–11719.
- 52. Lubberhuizen, W. H.; Vanmaekelbergh, D.; Fassen, E. V. Recombination of Photogenerated Charge Carriers in Nanoporous Gallium Phosphide. *J. Porous Mater.* **2000**, *7*, 147–152.
- 53. Frederikse, H. P. R. Recent Studies on Rutile (TiO₂). *J. Appl. Phys.* **1961**, *32*, 2211–2215.
- 54. Look, D. C.; Reynolds, D. C.; Sizelove, J. R.; Jones, R. L.; Litton, C. W.; Cantwell, G.; Harsch, W. C. Electrical Properties of Bulk ZnO. *Solid State Commun.* **1998**, *105*, 399–401.
- 55. Zhang, Q.; Dandeneau, C. S.; Zhou, X.; Cao, G. ZnO Nanostructures for Dye-Sensitized Solar Cells. *Adv. Mater.* **2009**, *21*, 4087–4108.